Exp. Theo. NANOTECHNOLOGY 10 (2026) 1337-1349 https://doi.org/10.56053/10.3.1337

Multitechnique characterization and antibacterial evaluation of Cr_2O_3 nanoparticles calcined at variable temperatures

Atheer. I. Abd Ali[1], *Zahraa Salah Ahmed*[1], *Mohammed RASHEED*[2,*], *Habiba Kadhim Aity*[3], *Hayder S. Ahmed*[4]

[1]Applied Sciences Department, University of Technology- Iraq, Baghdad 10066, Iraq
[2]College of Production Engineering & Metallurgy, University of Technology- Iraq, Baghdad, Iraq
[3]Scientific Research Commission, Baghdad, Iraq
[4]Electronic and Communication Department, Engineering College, University of Baghdad, Iraq
[*]) Email: rasheed.mohammed40@yahoo.com

Received 11/4/2026, *Received in revised form* 11/5/2026, *Accepted* 11/6/2026, *Published* 15/7/2026

Chromium(III) oxide nanoparticles (Cr_2O_3 NPs) were synthesized via a sol–gel method and calcined at 300, 400, and 500 °C to examine the influence of thermal treatment on structural, magnetic, and antibacterial properties. XRD confirmed the formation of phase-pure α- Cr_2O_3 at all temperatures, with enhanced crystallinity and reduced microstrain observed at 400 °C. Williamson–Hall analysis showed crystallite sizes of ~15.7 nm (300 °C), ~19.2 nm (400 °C), and ~14.9 nm (500 °C). FTIR spectra indicated progressive removal of residual hydroxyl and nitrate groups with increasing temperature, while TEM revealed improved particle uniformity at 400 °C. VSM analysis of Cr_2O_3 NPs calcined at 500 °C exhibited weak ferromagnetic behavior with a maximum magnetization of ~0.09 emu g^{-1}, remanent magnetization of ~0.025 emu g^{-1}, and low coercivity (~120), attributed to surface spin canting in the nanoparticles. Antibacterial studies against *Streptococcus pneumoniae* showed maximum inhibition at 400 °C, highlighting its optimal physicochemical and biological performance for biomedical applications.

Keywords: Cr_2O_3 NPs; XRD; TEM; VSM.

1. INTRODUCTION

Metal oxide nanoparticles are considered attractive multi-functional materials (physicochemical properties can be modified by changes in size and/ or shape among others) with a comparatively very high surface/mass ratio mainly for industrial, environmental as well as biomedical applications [1-4]. Among these materials, chromium(III) oxide (Cr_2O_3) nanoparticles have an upper hand due to its best thermal stability and mechanical hardness in addition to chemical inertness, corrosion resistance besides possibility antimicrobial activity [5, 6]. Novel antibacterial material is urgently needed because antibiotic resistant microbes are widely spread; nanomaterials based on oxides have drawn significant attention since they can deactivate bacterial membrane plus initiate contact reaction at the surface [7,8]. The metal oxide nanoparticles exhibit size dependent properties largely controlled by their structural parameters for example crystallite size lattice strain phase purity together with surface chemistry [9, 10]. The temperature of calcination controls these properties mainly through its influence of nucleation and grain growth, organics decomposition, defect annealing and particle sintering behavior thus necessitating a strict control over temperature in the process to be able to properly tune nanoparticles and increase their biological efficiency. Aside from the well-known Cr_2O_3 nanoparticles catalyst, magnetic materials, and antibacterial activities [14,15] few have reported temperature-driven structure and morphology changes of Cr_2O_3 nanoparticles. Also, no reliable relationship between crystallinity, microstrain, particle shape, and antibacterial activity exists. The best condition or heat treatment that favors the highest biological activities has not been discussed or explored yet [16,17].

More jointly comprehensive that breaks these relationships will also have to be considered [18,19]. Cr_2O_3 nanoparticles were synthesized by the solgel method then calcined at different temperatures. Thus, a systematic study of the influence of heat treatment on physicochemical properties and antibacterial activity for Cr_2O_3 nanostructures is enabled. Structural and morphological transformations have been interpreted in terms of X-ray diffractions, Williamson–Hall plot, FTIR, and TEM. Antibacterial screening against Streptococcus pneumoniae will use Agar diffusion and spread plate methods. Therefore, this research work tries to once again assert what has been already advanced by two-step sintering materials that grain size for lower Cr_2O_3 nanoparticle: based on consolidating the medicantness as compared to that found in biological performance.

2. MATERIALS AND METHODS

Chromium(III) oxide nanoparticles were synthesized by a sol–gel method using chromium(III) nitrate nonahydrate $Cr(NO_3)_3 \cdot 9H_2O$ (M = 400.15 g/mol) as the chromium precursor. To prepare a 0.10 M solution, 4.00 g of $Cr(NO_3)_3 \cdot 9H_2O$ was dissolved in 100 mL of distilled water under vigorous magnetic stirring until a clear green solution was obtained. To prevent the formation of $Cr(OH)_3$ precipitates and to stabilize the Cr^{3+} aquo complex $[Cr(H_2O)_6]^{3+}$, the pH of the solution was carefully adjusted to pH = 1.5 ± 0.1 by adding 2–3 drops of concentrated HNO_3 (M = 63.01 g/mol). Under these acidic conditions, the chromium ions remain solvated and undergo controlled hydrolysis.
The primary hydrolysis step is represented by [20, 21]:

$$[Cr(H_2O)_6]^{3+} \rightleftharpoons [Cr(H_2O)_5(OH)]^{2+} + H^+ \quad (1)$$

Continued stirring for 2 h promotes partial condensation of hydrolyzed species to form Cr–O–Cr linkages, initiating gel network formation [22, 23]:

$$2\,[Cr(H_2O)_5(OH)]^{2+} \rightarrow (H_2O)_5Cr - O - Cr(H_2O)_5^{4+} + H^+ \quad (2)$$

The resulting green sol was aged at room temperature to form a stable wet gel. The gel was dried at 100 °C for 12 h, removing adsorbed and coordinated water and forming a xerogel. The dehydration reaction may be written as [24, 25]:

$$Cr - OH + HO - Cr \rightarrow Cr - O - Cr + H_2O$$

(3)

The dried xerogel was ground into fine powder and divided into three equal portions. Each portion was calcined at 300, 400, or 500 °C for 3 h in a muffle furnace using a heating rate of 5 °C/min. During calcination, the chromium nitrate decomposes completely to α- Cr_2O_3, releasing gaseous byproducts. The main reaction is [26]:

$$2\,Cr(NO_3)_3.9H_2O \xrightarrow{\Delta} Cr_2O_3 + 6\,NO_2 + \frac{3}{2}O_2 + 18\,H_2O \quad (4)$$

The resulting nanopowders were labeled Cr_2O_3–300, Cr_2O_3–400, and Cr_2O_3–500. At 300 °C, the xerogel undergoes extensive dehydration and partial nitrate decomposition [27,28]:

$$Cr(NO_3)_3 \xrightarrow{300\,^oC} Cr(OH)_3 + NOx \quad (5)$$

$$2\,Cr(OH)_3 \rightarrow Cr_2O_3 + 3\,H_2O \quad (6)$$

The product is mostly amorphous, exhibiting very broad and weak XRD peaks due to incomplete crystallization and very small nanocrystal nuclei.

At 400 °C, nitrate removal is nearly complete, and the α- Cr_2O_3 phase develops [29, 30]:

$$2\,CrO(OH) \xrightarrow{400\,^oC} Cr_2O_3 + H_2O \quad (7)$$

Crystallinity increases significantly, although the particles remain nanometric and partially agglomerated. XRD reflections sharpen while retaining moderate peak broadening. At 500 °C, full conversion to highly crystalline α-Cr_2O_3 is achieved. Atomic mobility allows grain growth, reducing structural defects. XRD peaks become sharp and well defined, indicating high phase purity and nanocrystalline domain sizes [31,32].

$$Cr_2O_3\,(nanocrystalline) \xrightarrow{500\,^oC} Cr_2O_3\,(highly\ crystalline) \quad (8)$$

The phase composition, lattice parameters, and crystallite size of the Bi_2O_3 nanopowders were analyzed using a Bruker D8 Advance X-ray diffractometer with Cu Kα radiation (λ = 1.5406 Å), operated at 40 kV and 40 mA. Diffraction data were collected over a 2θ range of 20°–80° with a step size of 0.02°, and crystallite size, microstrain, and dislocation density were evaluated using Scherrer and Williamson–Hall methods. FTIR measurements were carried out using a Bruker Tensor 27 spectrometer in the 4000–400 cm^{-1} range to identify Bi–O vibrations and confirm the removal of residual organics. Magnetic properties were investigated at room temperature using a vibrating sample magnetometer (VSM) by recording hysteresis loops over an applied magnetic field range of ±10 kOe to determine saturation magnetization, remanent magnetization, and coercivity. Antibacterial activity was evaluated against *Escherichia coli* and *Staphylococcus aureus* using agar diffusion and spread plate methods. All experiments were performed in triplicate, and the results are reported as mean ± standard deviation, enabling correlation between structural, magnetic, and antibacterial properties [33-35].

3. RESULTS AND DISCUSSION

3.1. XRD

Figure 1 and Table 1 confirm that Cr_2O_3 nano-powders calcined at 300, 400, and 500 °C crystallize in a single-phase α-Cr_2O_3 structure with rhombohedral (trigonal) symmetry (space group R-3c, PDF 00-038-1479). All diffraction patterns exhibit characteristic peaks at 2θ ≈ 24.5°, 33.6°, 36.2°, 41.5°, 50.2°,

54.9°, 63.5–65.2°, and 72.8°, corresponding to the (012), (104), (110), (113), (024), (116), (214)/(300), and (10 10) planes of eskolaite-type Cr_2O_3. The absence of secondary phases confirms phase purity, while increased peak intensity at higher temperatures indicates improved crystallinity with minimal change in average crystallite size. Using Bragg's law [36-40]

$$n\lambda = 2dsin\theta \tag{9}$$

and the hexagonal interplanar spacing relation

$$\frac{1}{d_{hkl}^2} = \frac{4}{3}\frac{\left(h^2+hk+k^2\right)}{a^2} + \frac{l^2}{c^2} \tag{10}$$

The lattice parameters calculated from the most intense (104), (110), and (116) reflections are found to be a ≈ 4.95–4.97 Å and c ≈ 13.55–13.60 Å for all three samples. These values closely match the standard parameters of α-Cr_2O_3 (a = 4.958–4.959 Å, c = 13.59 Å) reported in the literature and the PDF reference, confirming the formation of a stable corundum-type structure. The absence of noticeable peak shifts with increasing calcination temperature indicates that the crystal structure, lattice symmetry, and unit-cell dimensions remain essentially unchanged between 300 and 500 °C, while crystallinity is significantly enhanced. With increasing calcination temperature, diffraction peaks become sharper and more intense with reduced background noise, reflecting improved crystallinity and decreased structural disorder; the 300 °C sample shows broader reflections characteristic of smaller coherent domains and higher microstrain, whereas the 500 °C sample exhibits well-defined peaks indicative of improved lattice ordering. The crystallite size D was estimated from the full width at half maximum (FWHM) of the diffraction peaks using the Scherrer equation, $D = K\lambda/(\beta cos\theta)$, where K is the shape factor (0.9), λ is the CuKα wavelength (0.15406 nm), β is the FWHM (in radians) corrected for instrumental broadening, and θ is the Bragg angle. As summarized in Table 1, the average crystallite sizes are ~22.0 nm (300 °C), ~20.3 nm (400 °C), and ~20.2 nm (500 °C). These small variations lie within the uncertainty of the Scherrer method, indicating that increased calcination temperature mainly reduces microstrain rather than causing significant grain growth. The combined XRD pattern for the Cr_2O_3 samples calcined at 300, 400 and 500 °C shows a series of well-defined diffraction peaks located at 2θ ≈ 24.5°, 33.6°, 36.2°, 41.5°, 50.2°, 54.9°, 63–65°, and 72–73°. These peaks have been indexed to the (012), (104), (110), (113), (024), (116), (214), (300) and (220) planes of α- Cr_2O_3 (eskolaite). The coincidence between the experimental peak positions and the reference lines confirms that all three powders are single-phase α- Cr_2O_3, with no additional peaks due to secondary phases or unreacted precursor [41-45].

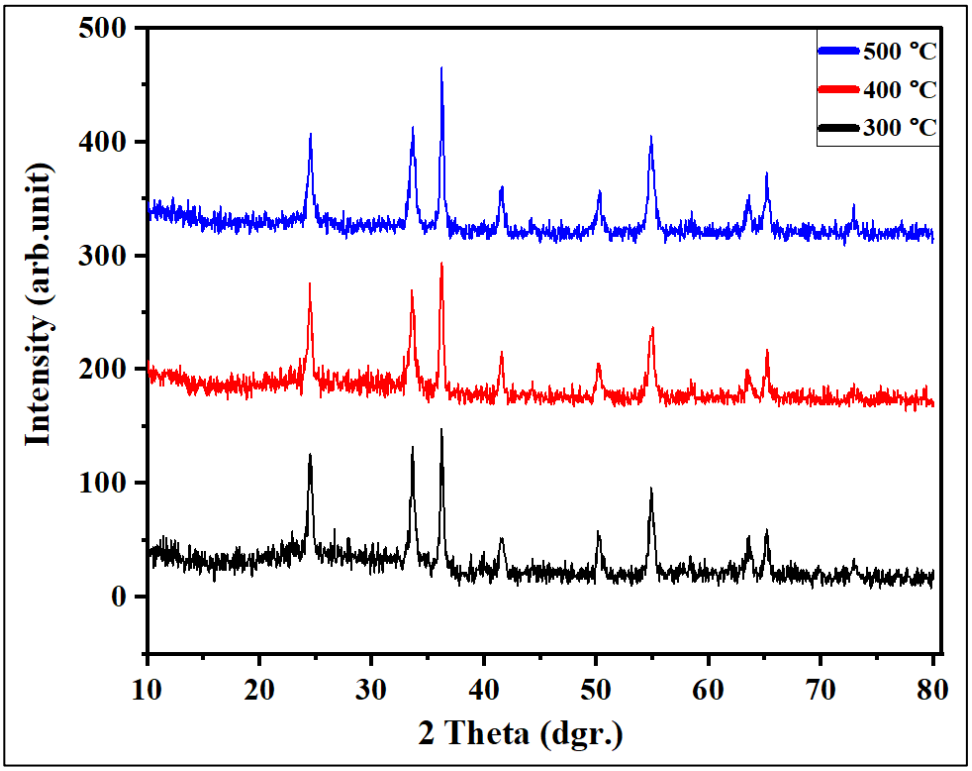

Figure 1 XRD pattern for the Cr_2O_3 NPs calcined at 300, 400 and 500 °C.

Table 1 XRD parameters for Cr_2O_3 NPs calcined at 300, 400 and 500 °C.

Sample	2Theata	FWHM	hkl	d-Spacing (A)	Crystallite size (nm)	D (nm) (Average)
Cr_2O_3 at 300 °C	24.5346	0.43460	(012)	3.62541	18.8545078	21.97980511
	33.6162	0.31250	(104)	2.66386	25.68765573	
	36.2363	0.29040	(110)	2.47703	27.44440615	
	41.5390	0.53750	(113)	2.17225	14.58733793	
	50.2128	0.41390	(024)	1.81546	18.34591715	
	54.8405	0.35370	(116)	1.67270	21.04476793	
	65.1348	0.30430	(214)	1.43101	23.22402442	
	74.7824	0.25000	(220)	1.26850	26.64982374	
Cr_2O_3 at 400 °C	24.5088	0.35910	(012)	3.62916	22.8197439	20.34587737
	33.6123	0.46630	(104)	2.66416	17.21525829	
	36.2029	0.35360	(110)	2.47924	22.54133283	
	41.5203	0.32500	(113)	2.17319	24.12670552	
	50.1864	0.41670	(024)	1.81635	18.22460912	
	54.8783	0.52920	(116)	1.67164	14.06322782	
	65.1954	0.24550	(214)	1.42983	28.77671091	
	72.7955	0.45000	(220)	1.29814	14.99943055	
Cr_2O_3 at 500 °C	24.5244	0.39500	(012)	3.62689	20.7451333	20.23069736
	33.6496	0.55420	(104)	2.66129	14.48337298	
	36.2441	0.31470	(110)	2.47651	25.3246839	
	41.5344	0.42540	(113)	2.17248	18.43162553	
	50.2306	0.34500	(024)	1.81486	22.00818067	
	54.8762	0.58580	(116)	1.67169	12.70455953	
	63.5023	0.49170	(300)	1.46381	14.50204943	
	65.1695	0.25080	(214)	1.43033	28.1726612	
	72.8517	0.26250	(220)	1.29728	25.70400972	

3.2. FTIR

Figure 2 shows the FTIR transmittance spectra of sol–gel–derived Cr_2O_3 nanoparticles calcined at 300, 400, and 500 °C over the range 400–4000 cm^{-1}. All samples exhibit the characteristic absorption band between 400 and 600 cm^{-1}, attributed to Cr–O stretching vibrations of CrO_6 octahedra in rhombohedral α-Cr_2O_3. This band becomes progressively sharper and more intense with increasing calcination temperature, indicating improved Cr–O–Cr network ordering and enhanced crystallinity. The 300 °C sample displays a broader and weaker Cr–O band, reflecting incomplete crystallization and higher structural disorder. Broad absorption features near ~3400 cm^{-1} and ~1630 cm^{-1}, corresponding to O–H stretching and H–O–H bending vibrations, are observed in all samples but decrease markedly with temperature, confirming the gradual removal of adsorbed moisture and hydroxyl species. Weak bands in the 1000–1500 cm^{-1} region, associated with residual nitrate species, are evident at 300 °C but diminish at higher temperatures. Overall, the FTIR results corroborate XRD findings, confirming

enhanced structural order and reduced residual impurities with increasing calcination temperature [46-50].

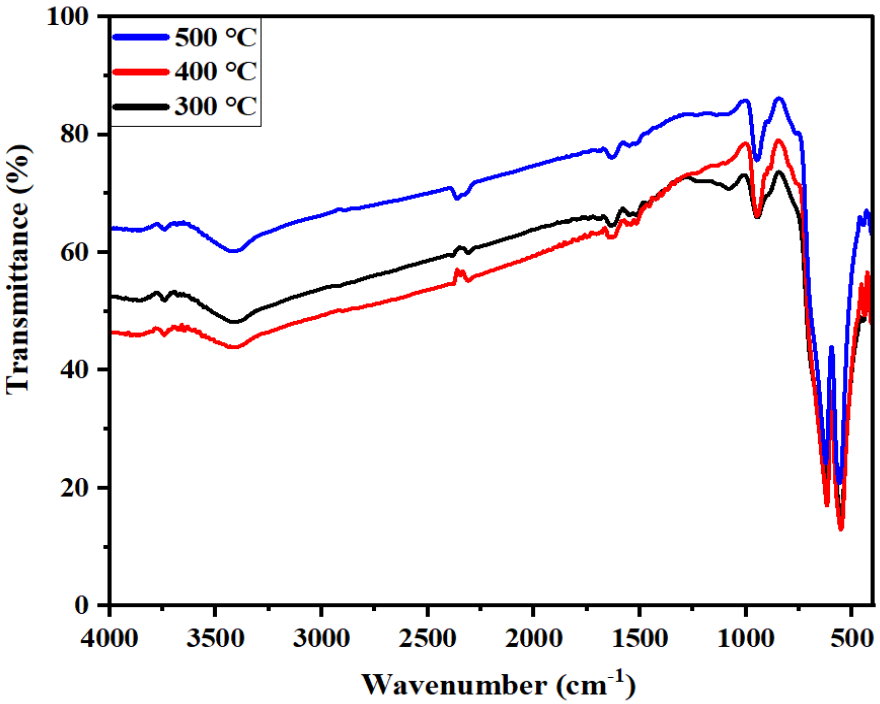

Figure 2 FTIR spectra of Cr_2O_3 NPs calcined at 300, 400, and 500 °C.

3.3. TEM

Figure 3 presents TEM micrographs of Cr_2O_3 nanoparticles calcined at 300, 400, and 500 °C, illustrating the influence of thermal treatment on particle morphology and crystallization. At 300 °C, the nanoparticles form heavily agglomerated clusters with poorly defined boundaries and irregular shapes, indicating incomplete crystallization and the presence of amorphous residues; particle sizes are mainly below 10–15 nm. At 400 °C, the particles exhibit clearer outlines, enhanced contrast, and improved dispersion, reflecting significantly higher crystallinity. The average particle size increases to ~15–20 nm, consistent with the maximum crystallite size obtained from Williamson–Hall analysis, while aggregation is noticeably reduced. At 500 °C, although high crystallinity is maintained, the particles form more compact aggregates due to the onset of thermal sintering, and the effective particle size decreases to ~10–15 nm. Particle-size distribution histograms (Figure 3 a1–c1) further confirm these trends, showing a shift toward larger, more uniform particles at 400 °C. Overall, TEM analysis confirms that 400 °C is the optimal calcination temperature for producing well-defined and uniformly sized Cr_2O_3 nanoparticles [51].

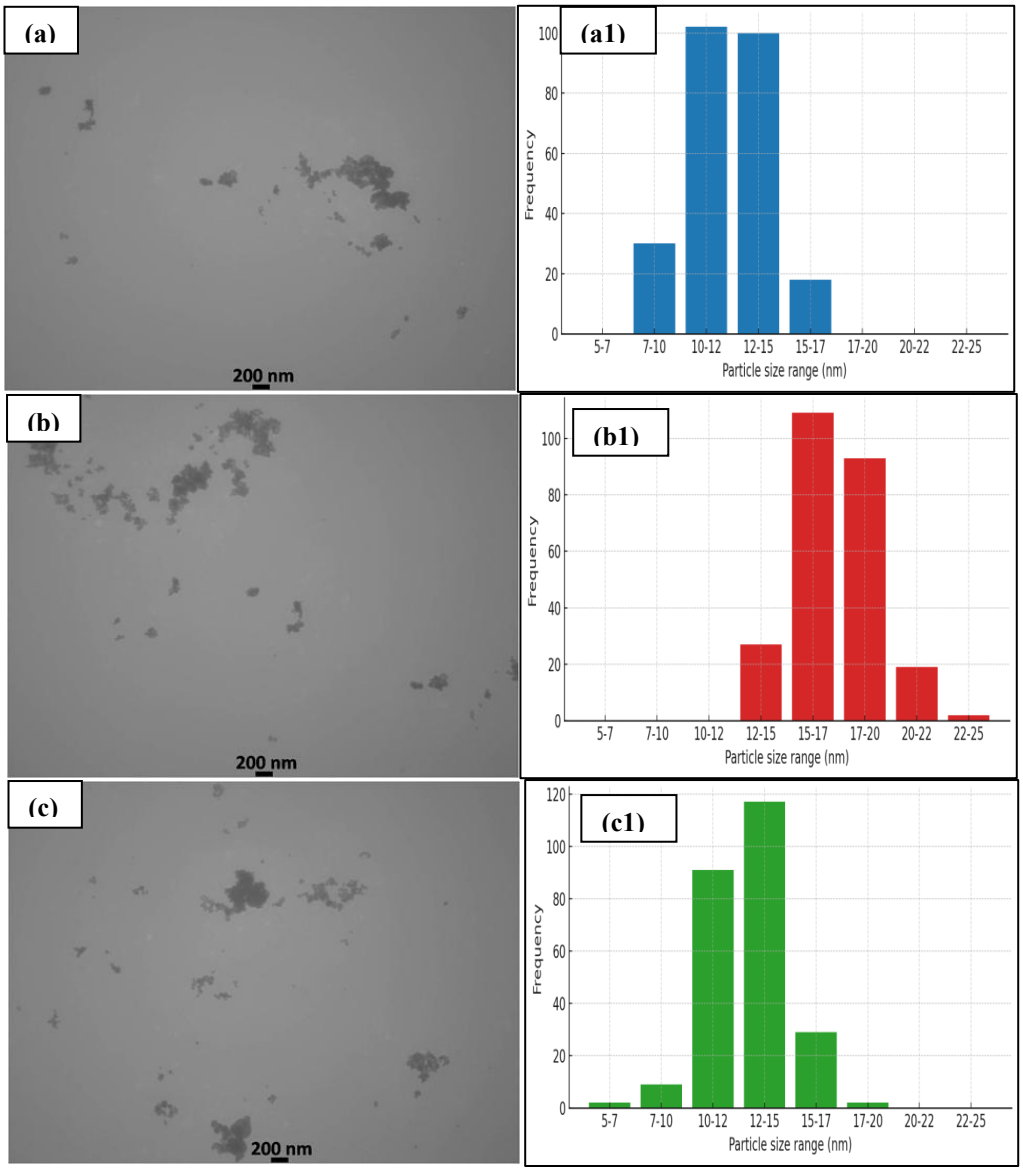

Figure 3 (a-c) the TEM micrographs of the Cr_2O_3 nanoparticles calcined at 300, 400, and 500 °C, and (a1–c1) histogram of the particle-size distributions.

3.4. Vibrating sample magnetometer (VSM)

The room-temperature VSM hysteresis loop of Cr_2O_3 nanoparticles annealed at 500 °C (Figure 4) exhibits a weak but distinct magnetic hysteresis, indicating the presence of a ferromagnetic-like component superimposed on an antiferromagnetic/paramagnetic background [52]. The maximum magnetization reaches approximately 0.09 emu g^{-1}, while the magnetization at the highest applied field remains unsaturated (~0.045 emu g^{-1}), confirming that the dominant magnetic nature of Cr_2O_3 is antiferromagnetic [53]. A small remanent magnetization of about 0.025 emu g^{-1} and a low coercive

field of ~120 (field units as applied) are observed, reflecting soft-magnetic behavior with easy magnetization reversal. The existence of finite coercivity and remanence in an otherwise antiferromagnetic oxide is commonly attributed to uncompensated surface spins, spin canting, and defects such as oxygen vacancies that become significant at the nanoscale. Annealing at 500 °C improves crystallinity and reduces magnetic disorder, yet retains surface-induced weak ferromagnetism, leading to the observed narrow hysteresis loop and non-saturating magnetization response [54, 55] (Figure 4).

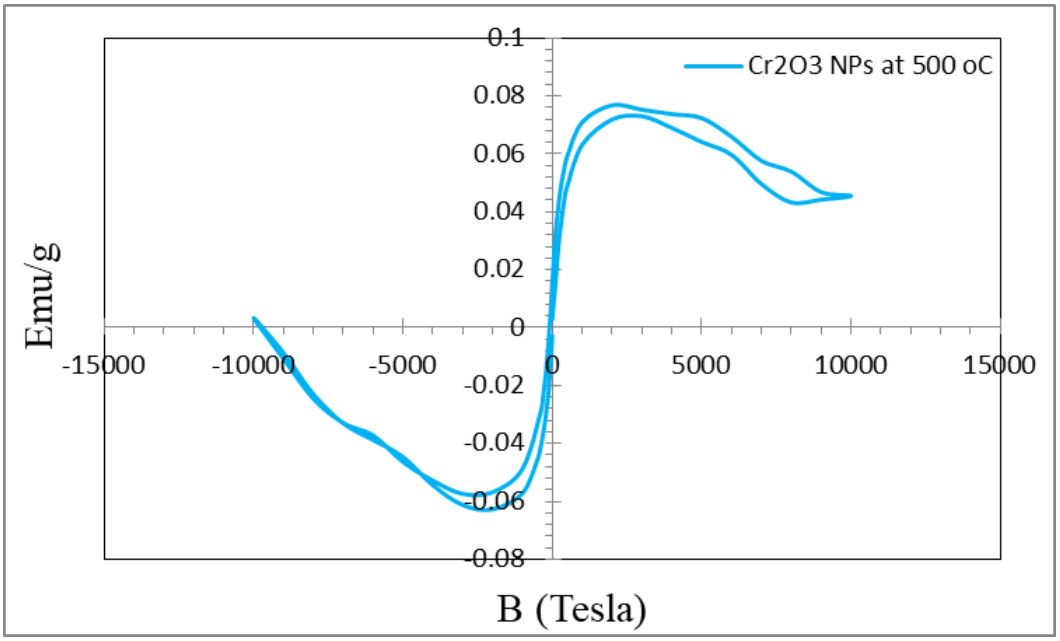

Figure 4 Room-temperature VSM hysteresis loop of Cr_2O_3 nanoparticles annealed at 500 °C.

3.5. Antibacterial activity
3.5.1. ADM

Figure 5 illustrates the antibacterial activity of Cr_2O_3 nanoparticles calcined at 300, 400, and 500 °C against *Streptococcus pneumoniae* as evaluated by the agar diffusion method. Clear inhibition zones are observed around all nanoparticle-loaded wells, confirming the antibacterial nature of Cr_2O_3. The nanoparticles calcined at 300 °C exhibit modest activity, producing an inhibition zone of 18 mm, which is attributed to incomplete crystallization, lower surface reactivity, and the presence of residual hydroxyl and nitrate groups. In contrast, the 400 °C sample shows the highest antibacterial efficiency, yielding a well-defined inhibition zone of 21 mm. This enhanced performance correlates with its optimal crystallite size, lowest microstrain, and uniform particle morphology, which promote stronger interactions with bacterial cell membranes. When the calcination temperature is increased to 500 °C, the inhibition zone decreases to 19 mm, indicating reduced antibacterial effectiveness [49, 50]. This decline is associated with thermally induced particle sintering and a reduction in available active surface sites [51]. Overall, these results clearly demonstrate that calcination at 400 °C produces Cr_2O_3 nanoparticles with superior antibacterial activity compared to those treated at lower or higher temperatures [56,57].

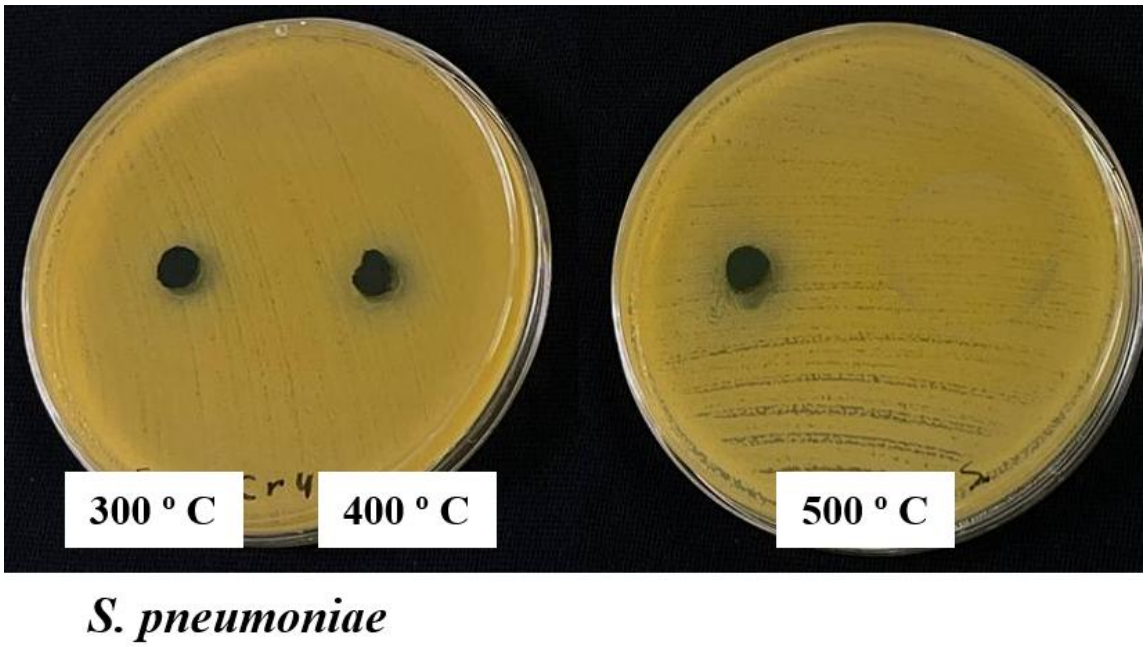

Figure 5 The antibacterial activity of Cr_2O_3 nanoparticles calcined at 300, 400, and 500 °C against *Streptococcus pneumoniae*, where the diameter of the inhibition zones demonstrates a strong dependence on calcination temperature, with the 400 °C sample producing the largest inhibitory effect.

Table 2 summarizes the antibacterial activity of Cr_2O_3 nanoparticles calcined at 300, 400, and 500 °C against *Streptococcus pneumoniae* using the agar diffusion method. A strong dependence of antibacterial performance on calcination temperature is evident. Nanoparticles calcined at 300 °C exhibit moderate activity, with a mean inhibition zone of 18.0 ± 1.0 mm, attributed to incomplete crystallization, smaller particle size, and residual surface hydroxyl and nitrate groups. In contrast, the 400 °C sample shows the highest antibacterial efficacy, producing a mean inhibition zone of 21.0 ± 1.0 mm. Statistical analysis confirms that this improvement is highly significant compared with 300 °C ($p = 0.003$) [52-55]. The enhanced activity at 400 °C correlates with optimal structural characteristics, including maximum crystallite size, lowest microstrain, and uniform particle morphology. The 500 °C sample yields an inhibition zone of 19.7 ± 0.6 mm, which remains statistically higher than the 300 °C sample ($p = 0.036$) but lower than that of the 400 °C sample. The slight reduction is attributed to thermal sintering and reduced surface reactivity. The optimal calcination temperature for antibacterial Cr_2O_3 nanoparticles is 400 °C [58,59].

Table 2 Antibacterial Activity of Cr_2O_3 NPs determined by the agar diffusion method (ADM)

Bacteria Type	Cr_2O_3 NPs (°C)	ADM Zone (mm) Rep 1	Rep 2	Rep 3	ADM Mean ± SD (mm)	t-value	p-value
S. pneumoniae	300 °C	17	18	19	18.0 ± 1.0	Reference	Reference
	400 °C	20	21	22	21.0 ± 1.0	4.24	0.003
	500 °C	19	20	20	19.7 ± 0.6	2.45	0.036

Notes: t-values and p-values compare each sample vs. the 300 °C reference group using a two-sample t-test, $p < 0.05$ = statistically significant, and $p < 0.01$ = highly significant.

3.5.2. SPM

Figure 6 illustrates the antibacterial activity of Cr_2O_3 nanoparticles calcined at 300, 400, and 500 °C against the Gram-positive bacterium *Streptococcus pneumoniae* using the spread plate method at a fixed nanoparticle mass of 0.3 g. The sample calcined at 300 °C shows five surviving bacterial colonies, indicating limited antibacterial effectiveness. This reduced activity is attributed to incomplete crystallization, smaller particle size, and the presence of residual hydroxyl and nitrate species that lower surface reactivity. In contrast, the Cr_2O_3 nanoparticles calcined at 400 °C demonstrate complete bacterial inhibition with zero detectable colonies, confirming the highest antibacterial potency among the tested samples. This enhanced performance correlates with optimal crystallinity, minimal microstrain, and an active nanoparticle surface [56-60]. For the sample calcined at 500 °C, five colonies are again observed, indicating a decline in antibacterial efficiency despite high crystallinity. This reduction is associated with thermally induced sintering and densification, which reduce the available surface area and active sites. Overall, Figure 18 clearly demonstrates that calcination at 400 °C yields Cr_2O_3 nanoparticles with superior antibacterial performance against *S. pneumonia* [60].

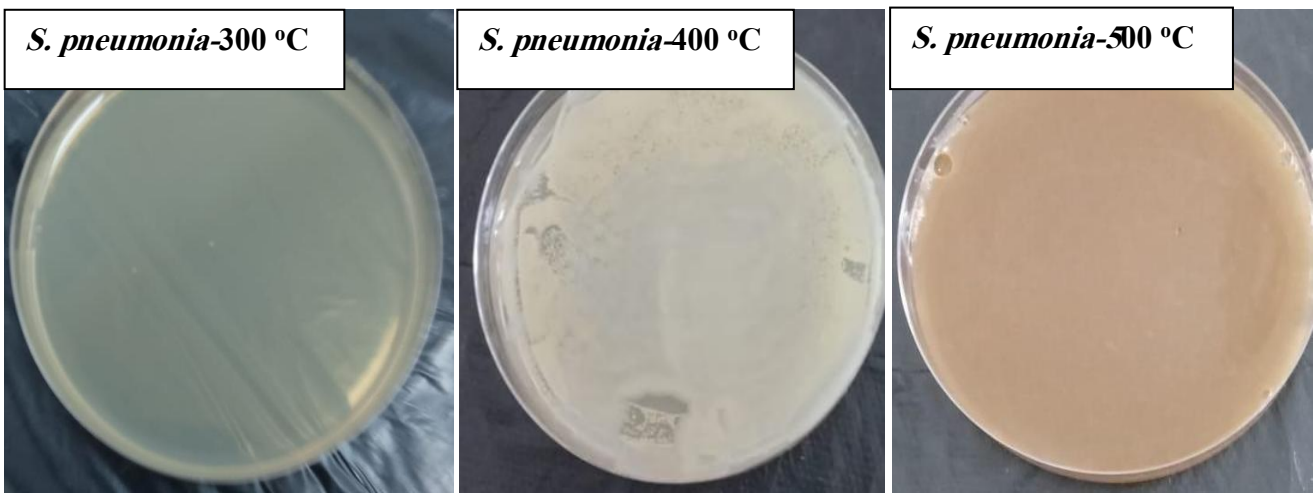

Figure 6 The antibacterial activity of Cr_2O_3 nanoparticles calcined at 300, 400, and 500 °C against *Streptococcus pneumoniae*.

Table 3 summarizes the antibacterial activity of Cr_2O_3 nanoparticles calcined at 300, 400, and 500 °C against *Streptococcus pneumoniae* as evaluated by the spread plate method, which quantitatively measures surviving bacterial colonies (CFU). The results clearly demonstrate that antibacterial performance is strongly dependent on calcination temperature. Nanoparticles calcined at 300 °C exhibit the highest bacterial survival, with a mean CFU value of 5.33 ± 0.58, indicating the weakest antibacterial activity [61-64]. This limited effectiveness is attributed to incomplete crystallization, elevated microstrain, and residual precursor species, which collectively reduce surface reactivity and hinder effective interaction with bacterial cell membranes. In contrast, the sample calcined at 400 °C shows near-complete bacterial inhibition, with a remarkably low mean CFU count of 0.33 ± 0.58. Statistical analysis confirms that this reduction is highly significant compared to the 300 °C sample ($t = -10.61$, $p = 0.00045$). The superior antibacterial performance at 400 °C correlates strongly with optimal physicochemical characteristics, including maximum crystallite size, minimal lattice strain, well-defined nanoparticle morphology, and an increased density of active surface sites. The nanoparticles calcined at 500 °C display intermediate activity, with a mean CFU of 3.67 ± 0.58 ($p = 0.024$ versus 300 °C), reflecting reduced efficacy due to thermal sintering and surface densification. The spread plate results confirm that 400 °C is the optimal calcination temperature for achieving maximal antibacterial activity, in agreement with XRD, TEM, and FTIR analyses [65-67].

Table 3 Antibacterial Activity of Cr_2O_3 NPs with different temperatures determined by spread plate method (SPM).

Bacteria Type	Cr_2O_3 NPs (°C)	CFU count or colonies Rep 1	Rep 2	Rep 3	SPM Mean ± SD (mm)	t-value	p-value
S. pneumoniae	300 °C	5	9	5	5.33 ± 0.58	Reference	Reference
	400 °C	0	0	1	0.33 ± 0.58	–10.61	0.00045
	500 °C	4	3	4	3.67 ± 0.58	–3.54	0.0241

Note: $p < 0.05$ → *statistically significant*, and $p < 0.01$ → *highly significant*

3.5.3. Materials chemistry perspective: Role of Cr_2O_3 NPs in enhancing antibacterial properties

From a materials chemistry perspective, the antibacterial performance of Cr_2O_3 nanoparticles is dictated by structure–property relationships that link crystallinity, particle size, surface chemistry, and defect density to bacterial interactions. At 300 °C, the nanoparticles are only partially crystallized, characterized by small coherent domains, high microstrain, and residual hydroxyl and nitrate species on the surface. This structural disorder limits the availability of well-coordinated Cr–O active sites and weakens nanoparticle adhesion to bacterial cell walls, resulting in reduced inhibition zones and higher CFU counts. Calcination at 400 °C yields nanoparticles with an optimal crystallite size of approximately 19 nm, minimal lattice strain, and a clean, well-ordered Cr–O framework, as confirmed by XRD, Williamson–Hall analysis, FTIR, and TEM. These features maximize accessible surface sites and promote strong interactions between exposed Cr^{3+}/O^{2-} terminations and the peptidoglycan-rich cell wall of Gram-positive *Streptococcus pneumoniae*, leading to membrane disruption and effective bacterial inactivation. At 500 °C, however, thermal sintering and particle coalescence reduce the effective surface area and introduce grain-boundary stresses that do not enhance antibacterial activity. Although the α- Cr_2O_3 phase is retained, increased densification limits nanoparticle–bacteria contact,

explaining the reduced antibacterial response relative to the 400 °C sample. Overall, optimal antibacterial performance arises from a carefully balanced nanostructure achieved at 400 °C rather than composition alone [1, 8].

4. CONCLUSIONS

This work establishes calcination temperature as a decisive factor in tailoring the structural, magnetic, and antibacterial properties of Cr_2O_3 nanoparticles. Structural analyses confirmed that calcination at 400 °C produces highly crystalline nanoparticles with minimal microstrain and uniform morphology, which directly correlates with superior antibacterial efficiency. Magnetic characterization of the sample calcined at 500 °C revealed weak ferromagnetic behavior, with a maximum magnetization of ~0.09 emu g^{-1}, remanent magnetization of ~0.025 emu g^{-1}, and low coercivity of ~120, originating from surface spin canting and uncompensated spins at the nanoscale. Although higher calcination enhances magnetic ordering, excessive thermal treatment leads to reduced surface activity due to particle densification, thereby diminishing antibacterial performance. Conversely, insufficient calcination results in defect-rich, poorly developed nanoparticles. The study demonstrates that a balanced thermal treatment at 400 °C optimizes physicochemical properties, while the observed magnetic behavior further confirms the nanoscale nature of Cr_2O_3, supporting its potential for multifunctional biomedical applications.

References

[1] A. Parveen, J. Cond. Matter, 3 (2025) 124. https://doi.org/10.61343/jcm.v3i02.70
[2] D. S. Silversmit et al., J. Sol–Gel Sci. Technol., 61 (2012) 61. https://doi.org/10.1016/j.ceramint.2020.06.185
[3] A. I. A. Ali, M. RASHEED, Experimental and Theoretical NANOTECHNOLOGY, 10 (2026) 239. https://doi.org/10.56053/10.s.239
[4] A. I. A. Ali, M. RASHEED, Experimental and Theoretical NANOTECHNOLOGY, 10 (2026) 277. https://doi.org/10.56053/10.s.277
[5] A. Khaleefah, M. RASHEED, Experimental and Theoretical NANOTECHNOLOGY, 10 (2026) 289. https://doi.org/10.56053/10.s.289
[6] F. Boudou, et al., Notulae Scientia Biologicae, 17 (2025) 12593. https://doi.org/10.55779/nsb17312593
[7] K. M. Parida, S. Singha, Appl. Surf. Sci., 256 (2025) 2670. https://doi.org/10.1016/j.apsusc.2024.162088
[8] I. Sondi, B. Salopek-Sondi, J. Colloid Interface Sci., 275 (2004) 177. https://doi.org/10.1016/j.jcis.2004.03.013
[9] I. M. Mohammed, M. Rasheed, AIP Conference Proceedings, 3321 (2025) 020026. https://doi.org/10.1063/5.0289719
[10] R. S. Mahmood, et al., Journal of the Mechanical Behavior of Materials, 34 (2025) 1. https://doi.org/10.1515/jmbm-2025-0040
[11] M. Rasheed, A. Khaleefah, Materials Chemistry and Physics, 355 (2026) 132112. https://doi.org/10.1016/j.matchemphys.2026.132112
[12] A. K. Geim, K. S. Novoselov, Nat. Mater., 6 (2021) 183. https://doi.org/10.32350/bsr.0303.01
[13] M. Rasheed, et al., Journal of Advanced Biotechnology and Experimental Therapeutics, 6 (2023) 495. https://doi.org/10.5455/jabet.2023.d144
[14] E. Kadri, et al., Journal of Alloys and Compounds, 705 (2017) 708. https://doi.org/10.1016/j.jallcom.2017.02.117

[15] M. Rasheed, R. Barillé, Journal of Alloys and Compounds, 728 (2017) 1186. https://doi.org/10.1016/j.jallcom.2017.09.084
[16] H. K. Aity, M. Rasheed, E. Dhahri, A. A. Hateef, T. Saidani, Journal of Materials Science, 61 (2026) 6226. https://doi.org/10.1007/s10853-026-12241-w
[17] S. S. Batros, M. Rasheed, H. K. Aity, A. A. Hatef, T. Saidani, Materials Chemistry and Physics, 355 (2026) 132243. https://doi.org/10.1016/j.matchemphys.2026.132243
[18] T. Saidani, M. Rasheed, I. Alshalal, A. A. Rashed, M. A. Sarhan, R. Barillé, Research on Engineering Structures and Materials, 9 (2023) 1. https://doi.org/10.17515/resm2023.21ma0922rs
[19] M. Rasheed, O. Y. Mohammed, S. Shihab, A. Al-Adili, Journal of Physics: Conference Series, 1795 (2021) 012042. https://doi.org/10.1088/1742-6596/1795/1/012042
[20] A. Raghdi, M. Heraiz, M. Rasheed, A. Keziz, Journal of the Indian Chemical Society, 101 (2024) 101413. https://doi.org/10.1016/j.jics.2024.101413
[21] F. Boudou, A. E. Sabar, M. I. Majeed, A. M. Ibraham, R. Jamal, A. Rashid, A. Belakredar, M. Bendahmane-Salmi, M. RASHEED, R. RASHEED, T. Saidani, H. D. Al-Bahadli, Experimental and Theoretical NANOTECHNOLOGY, 10 (2026) 821. https://doi.org/10.56053/10.S.821
[22] D. Kherifi, A. Keziz, M. Rasheed, A. Oueslati, Ceramics International, 50 (2024) 1. https://doi.org/10.1016/j.ceramint.2024.05.317
[23] M. Rasheed, S. Shihab, O. Alabdali, A. Rashid, T. Rashid, Journal of Physics: Conference Series, 1999 (2021) 012077. https://doi.org/10.1088/1742-6596/1999/1/012077
[24] K. K. Khudair, F. Boudou, A. Mohammed, A. Sehmi, A. Belakredar, M. S. Ibrahim, Experimental and Theoretical NANOTECHNOLOGY, 10 (2026) 869. https://doi.org/10.56053/10.S.869
[25] E. Kadri, M. Krichen, R. Mohammed, A. Zouari, K. Khirouni, Optical and Quantum Electronics, 48 (2016) 1. https://doi.org/10.1007/s11082-016-0812-7
[26] M. Rai, A. Yadav, A. Gade, Biotechnol. Adv., 27 (2009) 76. https://doi.org/10.1016/j.biotechadv.2008.09.002
[27] H. K. Aity, E. Dhahri, M. Rasheed, Ceramics International, 50 (2024) 54666. https://doi.org/10.1016/j.ceramint.2024.10.324
[28] S. P. Dubey, M. Lahtinen, M. Sillanpää, Collo. Sur. A: Phys. Eng. Asp, 364 (2010) 34. https://doi.org/10.1016/j.colsurfa.2010.05.033
[29] Y. K. Shin, H. Kwak, A. V. Vasenkov, D. Sengupta, A. C. T. van Duin, ACS Cataly. 5 (2015) 7226. https://doi.org/10.1021/acscatal.5b01766
[30] M. S. Ibrahim, T. T. Issa, B. Yaqoob, E. N. Fayyadh, A. Rashid, R. S. Mahmood, Experimental and Theoretical NANOTECHNOLOGY, 10 (2026) 887. https://doi.org/10.56053/10.S.887
[31] Z. S. Ahmed, M. RASHEED, H. S. Ahmed, Experimental and Theoretical NANOTECHNOLOGY, 10 (2026) 329. https://doi.org/10.56053/10.s.329
[32] Z. S. Ahmed, M. RASHEED, H. S. Ahmed, Experimental and Theoretical NANOTECHNOLOGY, 10 (2026) 343. https://doi.org/10.56053/10.s.343
[33] E. Arif, R. Jamal, M. RASHEED, Experimental and Theoretical NANOTECHNOLOGY, 10 (2026) 453. https://doi.org/10.56053/10.2.453
[34] G. E. Alkinani, A. R. J. Katae, M. RASHEED, Experimental and Theoretical NANOTECHNOLOGY, 10 (2026) 1027. https://doi.org/10.56053/10.S.1027
[35] A. Keziz, M. Rasheed, M. Heraiz, F. Sahnoune, A. Latif, Ceramics International, 49 (2023) 37423. https://doi.org/10.1016/j.ceramint.2023.09.068
[36] A. A. Hateef, E. Dhahri, M. Rasheed, H. Kadhim, Z. Abbas, N. Hassan, Physics and Chemistry of Solid State, 25 (2024) 801. https://doi.org/10.15330/pcss.25.4.801-810
[37] T. Saidani, S. Mokhtari, M. Rasheed, H. Lahmar, M. Trari, Journal of the Indian Chemical Society, 103 (2026) 102499. https://doi.org/10.1016/j.jics.2026.102499

[38] A. J. Hussein, M. N. Al-Darraji, M. Rasheed, IOP Conference Series: Earth and Environmental Science, 1262 (2023) 022007. https://doi.org/10.1088/1755-1315/1262/2/022007
[39] A. Ahmed, M. A. Salam, A. A. El-Sayed, J. Inorg. Organomet. Polym., 28 (2018) 2418. https://doi.org/10.62441/nano-ntp.v20is7.37
[40] M. A. Valenzuela, P. Bosch, T. López, J. Mol. Catal. A Chem., 167 (2017) 103. https://doi.org/10.1016/j.matchemphys.2017.09.047
[41] T. Rashid, M. M. Mokji, M. Rasheed, Journal of Optics, 53 (2024) 1. https://doi.org/10.1007/s12596-024-02080-w.
[42] A. A. Abdulrahman, M. Rasheed, S. Shihab, Journal of Physics: Conference Series, 1879 (2021) 022118. https://doi.org/10.1088/1742-6596/1879/2/022118
[43] T. Rashid, M. M. Mokji, M. Rasheed, Journal of the Mechanical Behavior of Materials, 34 (2025) 1. https://doi.org/10.1515/jmbm-2025-0074
[44] M. Enneffati, M. Rasheed, B. Louati, K. Guidara, R. Barillé, Optical and Quantum Electronics, 51 (2019) 1. https://doi.org/10.1007/s11082-019-2015-5
[45] A. Jaber, M. Ismael, T. Rashid, M. A. Sarhan, M. Rasheed, I. M. Sala, Eureka: Physics and Engineering, 4 (2023) 29. https://doi.org/10.21303/2461-4262.2023.002770
[46] A. J. Hussein, M. N. Al-Darraji, M. Rasheed, M. A. Sarhan, IOP Conference Series: Earth and Environmental Science, 1262 (2023) 022005. https://doi.org/10.1088/1755-1315/1262/2/022005
[47] M. Rasheed, I. Alshalal, A. A. Rashed, M. A. Sarhan, A. S. Jaber, Indonesian Journal of Electrical Engineering and Computer Science, 33 (2024) 653. https://doi.org/10.11591/ijeecs.v33.i1.pp653-660
[48] M. Rasheed, M. N. Mohammedali, F. A. Sadiq, M. A. Sarhan, T. Saidani, Journal of Optics, 54 (2024) 1. https://doi.org/10.1007/s12596-024-01928-5
[49] A. R. J. Katae, H. H. Hussein, A. S. Jaber, M. A. Sarhan, M. RASHEED, Experimental and Theoretical NANOTECHNOLOGY, 10 (2026) 795. https://doi.org/10.56053/10.2.795
[50] A. R. J. Katae, H. H. Hussein, A. S. Jaber, M. A. Sarhan, M. RASHEED, Experimental and Theoretical NANOTECHNOLOGY, 10 (2026) 725. https://doi.org/10.56053/10.2.725
[51] H. M. I. Al-Zuhairi, I. Alshalal, H. H. Abbood, M. Al Nuaimi, Experimental and Theoretical NANOTECHNOLOGY, 10 (2026) 855. https://doi.org/10.56053/10.S.855
[52] H. M. I. Al-Zuhairi, I. Alshalal, H. H. Abbood, M. Al Nuaimi, Experimental and Theoretical NANOTECHNOLOGY, 10 (2026) 1093. https://doi.org/10.56053/10.S.1093
[53] W. Saidi, N. Hfaidh, M. Rasheed, M. Girtan, A. Megriche, M. El Maaoui, RSC Advances, 6 (2016) 68819. https://doi.org/10.1039/c6ra15060h
[54] A. Zubaidi, L. M. Asaad, I. Alshalal, M. Rasheed, Journal of the Mechanical Behavior of Materials, 32 (2023) 1. https://doi.org/10.1515/jmbm-2022-0302
[55] M. Enneffati, B. Louati, K. Guidara, M. Rasheed, R. Barillé, Journal of Materials Science: Materials in Electronics, 29 (2018) 171. https://doi.org/10.1007/s10854-017-7901-7
[56] F. Dkhilalli, S. Megdiche, K. Guidara, M. Rasheed, R. Barillé, M. Megdiche, Ionics, 24 (2018) 169. https://doi.org/10.1007/s11581-017-2193-8
[57] F. Boudou, A. Guendouzi, A. Belakredar, M. RASHEED, Notulae Scientia Biologicae, 16 (2024) 13837. https://doi.org/10.55779/nsb16211837
[58] F. Boudou, A. Belakredar, A. Berkane, M. RASHEED, Notulae Scientia Biologicae, 17 (2025) 12183. https://doi.org/10.55779/nsb17212183
[59] A. Aukštuolis, et al., Proceedings of the Romanian Academy Series A: Mathematics, Physics, Technical Sciences, Information Science, 18 (2017) 34. https://hal.archives-ouvertes.fr/hal-02443179
[60] T. Saidani, M. Zaabat, M. S. Aida, R. Barillé, M. Rasheed, Y. Almohamed, Journal of Materials Science: Materials in Electronics, 28 (2017) 9252. https://doi.org/10.1007/s10854-017-6660-9

Exp. Theo. NANOTECHNOLOGY 10 (2026) 1337-1349